



Article

Investigations of $\text{LiNb}_{1-x}\text{Ta}_x\text{O}_3$ Nanopowders Obtained with Mechanochemical Method

Leonid Vasylechko ¹, Volodymyr Sydoruk ², Andrey Lakhnik ³, Yuriy Suhak ⁴, Damian Wlodarczyk ⁵ , Stepan Hurskyi ^{1,4}, Uliana Yakhnevych ^{1,*}, Yaroslav Zhydachevskyy ^{1,5} , Dmytro Sugak ^{1,6}, Ihor I. Syvorotka ⁶, Ivan Solskii ⁶, Oleh Buryi ¹, Andrzej Suchocki ⁵ and Holger Fritze ⁴

¹ Department of Semiconductor Electronics, Lviv Polytechnic National University, 12, Bandery Str., 79013 Lviv, Ukraine; crystal-lov@polynet.lviv.ua (L.V.); stepan.hurskyi@tu-clausthal.de (S.H.); zhydach@ifpan.edu.pl (Y.Z.); dm_sugak@yahoo.com (D.S.); oburyi@yahoo.com (O.B.)

² Institute for Sorption and Problems of Endoecology, NASU, 13 Gen. Naumov St., 03164 Kyiv, Ukraine; bilychi@ukr.net

³ G.V. Kurdyumov Institute of Metal Physics NASU, 36 Acad. Vernadsky Bvd., 03142 Kyiv, Ukraine; lakhnik@imp.kiev.ua

⁴ Institute for Energy Research and Physical Technologies, Clausthal University of Technology, Am Stollen 19B, 38640 Goslar, Germany; sensorik@tu-clausthal.de (Y.S.); sensorikK@tu-clausthal.de (H.F.)

⁵ Division of physics and technology of wide-band-gap semiconductor nanostructures, Institute of Physics PAS, 32/46 Al. Lotników, 02668 Warsaw, Poland; wlodar@ifpan.edu.pl (D.W.); suchy@ifpan.edu.pl (A.S.)

⁶ Scientific Research Company 'Electron-Carat', 202 Stryjska St., 79031 Lviv, Ukraine; ii.syvorotka@carat.electron.ua (I.I.S.); solskii@carat.lviv.ua (I.S.)

* Correspondence: uliana.v.yakhnevych@lpnu.ua



Citation: Vasylechko, L.; Sydoruk, V.; Lakhnik, A.; Suhak, Y.; Wlodarczyk, D.; Hurskyi, S.; Yakhnevych, U.; Zhydachevskyy, Y.; Sugak, D.; Syvorotka, I.I.; et al. Investigations of $\text{LiNb}_{1-x}\text{Ta}_x\text{O}_3$ Nanopowders Obtained with Mechanochemical Method. *Crystals* **2021**, *11*, 755. <https://doi.org/10.3390/cryst11070755>

Academic Editors: László Kovács and Gábor Corradi

Received: 21 May 2021

Accepted: 25 June 2021

Published: 28 June 2021

Publisher's Note: MDPI stays neutral with regard to jurisdictional claims in published maps and institutional affiliations.



Copyright: © 2021 by the authors. Licensee MDPI, Basel, Switzerland. This article is an open access article distributed under the terms and conditions of the Creative Commons Attribution (CC BY) license (<https://creativecommons.org/licenses/by/4.0/>).

Abstract: Nanocrystalline compounds $\text{LiNb}_{1-x}\text{Ta}_x\text{O}_3$ of various compositions ($x = 0, 0.25, 0.5, 0.75, 1$) were synthesized by high-energy ball milling of the initial materials ($\text{Li}_2\text{CO}_3, \text{Nb}_2\text{O}_5, \text{Ta}_2\text{O}_5$) and subsequent high-temperature annealing of the resulting powders. Data on the phase composition of the nanopowders were obtained by X-ray diffraction methods, and the dependence of the structural parameters of $\text{LiNb}_{1-x}\text{Ta}_x\text{O}_3$ compounds on the value of x was established. As a result of the experiments, the optimal parameters of the milling and annealing runs were determined, which made it possible to obtain single-phase compounds. The Raman scattering spectra of $\text{LiNb}_{1-x}\text{Ta}_x\text{O}_3$ compounds ($x = 0, 0.25, 0.5, 0.75, 1$) have been investigated. Preliminary experiments have been carried out to study the temperature dependences of their electrical conductivity.

Keywords: nanoparticles; nanopowders; lithium niobate-tantalate; X-ray diffraction; Raman spectroscopy; temperature dependence of electroconductivity

1. Introduction

Lithium niobate (LiNbO_3 , LN) and tantalate (LiTaO_3 , LT) are among the most studied oxide compounds in modern materials science. This interest is due to the widest application of these materials in functional electronics. Analytical studies of the global market for LN and LT sales performed by various marketing agencies [1–4] show that as of the end of 2020, their consumption in monetary terms exceeded \$40 billion per year, and by 2027, it may reach more than \$75 billion. Such impressive sales are due to the variety of electronics industry branches and devices that use LN and LT. Accordingly, the forms in which these materials are used in practice are also different—single crystals, thin films, micro- and nanopowders, ceramics. Moreover, they can have a different chemical composition—congruent, stoichiometric, and contain various dopants of metal ions. It is obvious that such a variety of forms and applications again requires research to modify and optimize material properties.

$\text{LiNb}_{1-x}\text{Ta}_x\text{O}_3$ (LN-LT) solid solutions have recently been studied (see, for example, [5–8]), while they open up prospects for combining the advantages of both materials.

In particular, the LN-LT can be expected to exhibit high piezoelectric coefficients (close to LN) and the temperature stability of the LT properties. However, the growth of LN-LT single crystals is challenging because of the deviation from stoichiometry inherent in LN and LT crystals, the uneven distribution of cations caused by fluctuations in the temperature fields in the crystal growth zone, and differences in the melting temperatures T_m of both end components of the system ($T_m(\text{LiNbO}_3) = 1240\text{ }^\circ\text{C}$; $T_m(\text{LiTaO}_3) = 1650\text{ }^\circ\text{C}$).

Meanwhile, LN-LT nanoparticles can be attractive both for practical application and from the point of view of fundamental research, for example, to determine the dependence of the $\text{LiNb}_{1-x}\text{Ta}_x\text{O}_3$ structural characteristics depending on the composition.

Today, wet chemistry methods are most commonly used to obtain LN and LT nanoparticles. Among them, the sol-gel method predominates, when Nb or Ta pentaetoxides and Li ethoxide or salts—acetates, citrates, nitrates [1–5,9–14]—are chosen as starting materials for obtaining xerogels. Since alcoxides are extremely sensitive to moisture and susceptible to hydrolysis, the entire synthesis procedure must be carried out in a box filled with pure dry N_2 or Ar. In [7,15], LN nanoparticles were synthesized by the sol-gel method using a solution of NbCl_5 in toluol and LiNO_3 as starting materials. However, even in this case, part of the technological operations must be performed in a dry N_2 or Ar environment. In addition, in the sol-gel method, NbF_5 or TaF_5 , obtained by the action of HF on niobium and tantalum oxides, can be used as starting materials (see, e.g., [16,17]).

Another method to obtain LN nanoparticles is the solution combustion method. For example, the authors of [18] have successfully synthesized LiNbO_3 and $\text{LiNbO}_3\text{:Fe}$ nanopowders. The starting materials were LiNO_3 , aqueous iron nitrate $\text{Fe}(\text{NO}_3)_3 \cdot 9\text{H}_2\text{O}$, ammonium niobium (V) oxalate hydrate $\text{C}_4\text{H}_4\text{NNbO}_9 \cdot n\text{H}_2\text{O}$, and glycine $\text{C}_2\text{H}_5\text{NO}_2$. After mixing and long stirring of the starting materials, a precursor was formed, which was calcinated at a temperature of $600\text{ }^\circ\text{C}$ for 1 h in an O_2 atmosphere.

Another wet method is solvothermal synthesis, which was used to obtain LiTaO_3 nanopowders [19]. The authors used an autoclave, 80% of the volume of which was filled with a Li_2CO_3 solution in a mixture of distilled water and glycol with the addition of an appropriate amount of Ta_2O_5 . The autoclave was kept at $240\text{ }^\circ\text{C}$, and the contents were constantly stirred for 12 h under autogenous pressure. The resulting LT nanopowders were washed, centrifuged, and calcinated.

The preparation of LN and LT nanoparticles by wet chemistry shows that there are certain difficulties in their application. First of all, this is the multistage nature of technological processes (dissolution, mixing, stirring, centrifugation, high-temperature treatment, calcination, etc.): the use of a large number of organic and inorganic reagents, including hazardous; performing synthesis in a special environment; use of relatively high temperatures. These factors make the process of obtaining nanoparticles time-consuming and expensive. In addition, an increase in the number of technological operations and the number of reagents used increases the probability of errors in the synthesis. Finally, the production of nanopowders in large quantities is complicated using the methods described above.

In contrast to wet chemistry methods, high-energy ball milling with subsequent annealing of powders looks promising from a technological point of view with relatively simple production organization. The synthesis process consists of only two stages—milling and subsequent annealing, which could be performed in air. Only Li_2CO_3 , Nb_2O_5 , and Ta_2O_5 can be used as starting materials. Today, we are aware of only three works that describe the successful synthesis of LN nanopowders by the mechanochemical method [20–22].

In addition, in [23,24], in order to obtain nanocrystals of lithium niobate, the preliminary synthesized LiNbO_3 phase was milled. In [23], LN obtained by the solid-phase reaction between lithium carbonate and niobium pentoxide was subjected to milling. In [24], the remnants of the melt solidified in the crucible after the completion of the procedure for growing the LN single crystal by the Czochralski method were used for milling. To the best of our knowledge, there are no works devoted to the mechanochemical

synthesis of LT nanopowders. Furthermore, the synthesis and properties of nanopowders of $\text{LiNb}_{1-x}\text{Ta}_x\text{O}_3$ solid solutions, with $0 < x < 1$, remain completely unexplored.

This work focuses on the preparation of $\text{LiNb}_{1-x}\text{Ta}_x\text{O}_3$ nanopowders of different compositions ($x = 0, 0.25, 0.5, 0.75, 1$), using the mechanochemical synthesis method (high-energy ball milling of the starting materials Li_2CO_3 , Nb_2O_5 , Ta_2O_5 and subsequent annealing). Furthermore, the crystal structure, Raman spectra, and electrophysical properties of obtained LN-LT compounds are studied.

2. Materials and Methods

The mixed lithium niobate–tantarate nanopowders with nominal compositions $\text{LiNb}_{1-x}\text{Ta}_x\text{O}_3$ ($x = 0, 0.25, 0.5, 0.75$ and 1) were obtained by high-energy ball milling mixtures of Li_2CO_3 , Nb_2O_5 , and Ta_2O_5 powders (manufactured by Alfa Aesar, purity 4N) taken in molar ratios corresponding to stoichiometric compositions. The masses of the components for obtaining compounds with a certain x value are given in Table 1.

Table 1. Weights of reagents Li_2CO_3 , Nb_2O_5 , and Ta_2O_5 , calculated to obtain 10 g of stoichiometric compounds $\text{LiNb}_{1-x}\text{Ta}_x\text{O}_3$.

Sample No.	Composition	Weight, g		
		Li_2CO_3	Nb_2O_5	Ta_2O_5
S01 ($x = 0$)	LiNbO_3	2499	8989	–
S02 ($x = 0.25$)	$\text{LiNb}_{0.75}\text{Ta}_{0.25}\text{O}_3$	2175	5868	3252
S03 ($x = 0.5$)	$\text{LiNb}_{0.5}\text{Ta}_{0.5}\text{O}_3$	1926	3463	5758
S04 ($x = 0.75$)	$\text{LiNb}_{0.25}\text{Ta}_{0.75}\text{O}_3$	1727	1554	7748
S05 ($x = 1$)	LiTaO_3	1566	–	9367

The synthesis was performed with the planetary ball mill machine Pulverisette-7. The rotation speed was equal to 600 rpm, and the duration of milling was about 10–15 h. A total of 134 balls of zirconium dioxide with a diameter of 5 mm and total weight of 91.5 g were used as working bodies. The mass ratio ball/sample was about 10. Milling was performed in 15 min cycles; subsequently, a reverse was carried out after each cycle. Based on the results of previous investigations (see, e.g., [21] where LiNbO_3 nanoparticles were synthesized by a mechanochemical technique), one can assume that the surfaces of particles are activated, but the synthesis exactly of an LN-LT compound was not fully completed after milling. This is confirmed by X-ray analysis of the powders performed after milling. As an example, Figure 1 shows a diffraction pattern of a powder with $x = 0.5$ compared to the reference pattern of a lithium niobate powder from the PDF database. The results of X-ray phase analysis indicate the formation of a predominantly amorphous precursor and partially a perovskite-like phase of lithium niobate.

To obtain nanocrystalline LN-LT particles, subsequent annealing of powders was performed. To determine the range for selecting the optimal annealing temperature, thermal analysis curves of the powders after milling were recorded. These dependences for all samples had a similar character. As an example, Figure 2 shows the thermogravimetric curves for milled mixture corresponding to $\text{LiNb}_{0.5}\text{Ta}_{0.5}\text{O}_3$ powder. As can be seen, sharp mass loss is observed within 400–550 °C (TG and DTG curves). This event corresponds to the decomposition of lithium carbonate according to (1):



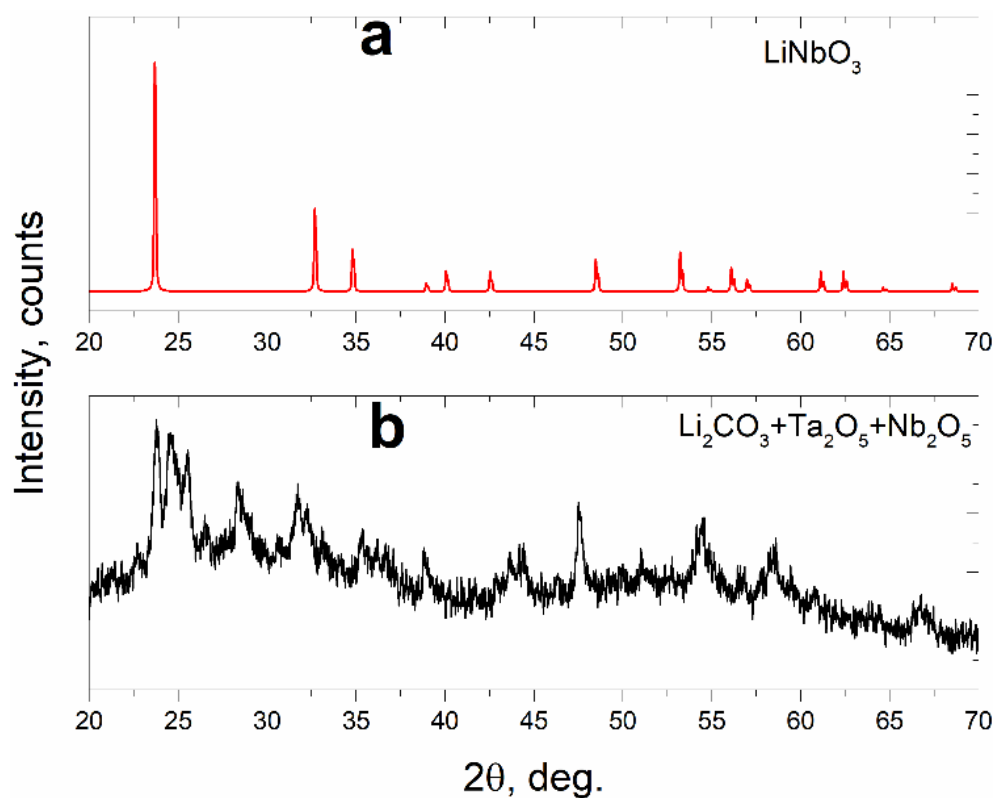


Figure 1. Reference diffraction patterns of lithium niobate (a) and diffraction patterns of the precursor obtained after milling a mixture of powders of lithium carbonate, niobium pentoxide, and tantalum pentoxide (b).

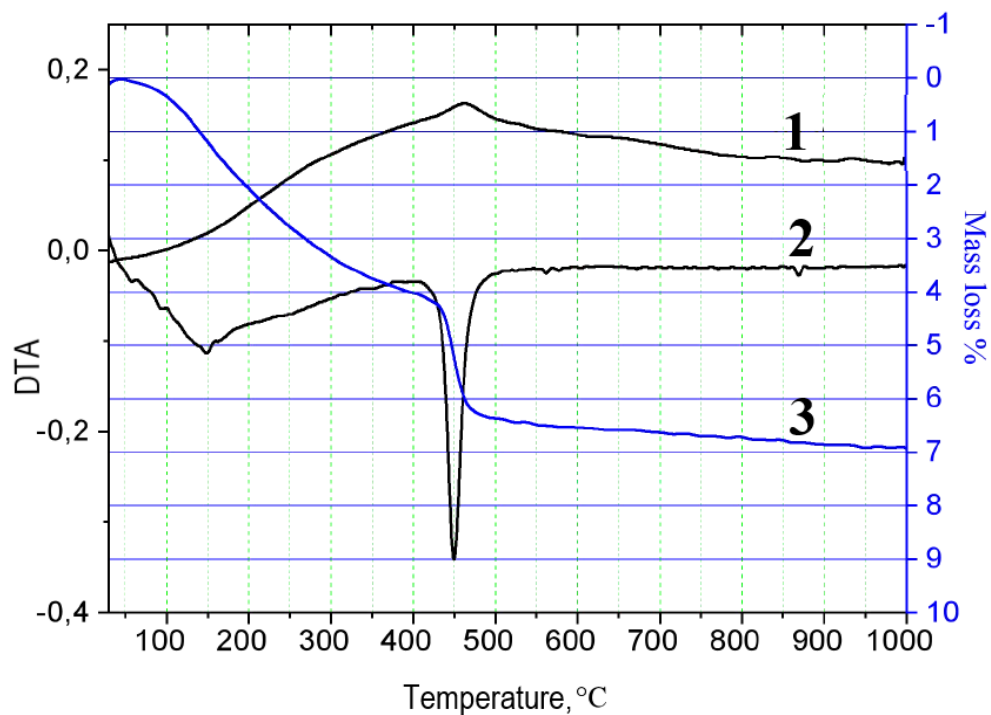
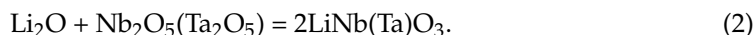


Figure 2. DTA–DTG curves obtained for $\text{LiNb}_{0.5}\text{Ta}_{0.5}\text{O}_3$ powders, which underwent a high-energy ball milling process for 15 h at a rotation speed of 600 rpm (1—DTA; 2—DTG; 3—TG).

At the same time, it is known that lithium carbonate decomposes above 800 °C [25]. Therefore, significant lowering of the temperature of this process is observed after milling the reaction mixture. In addition, the experimental value of mass loss in the temperature range 400–550 °C is about 20% of the theoretical value calculated by (1). The latter indicates that about 80% of lithium carbonate is decomposed at the stage of milling. Above 550 °C, the interaction of the formed lithium oxide with niobium (tantalum) oxides according to Reaction (2) occurs:



Based on the obtained results, three annealing temperatures in air were chosen for the experiments—550, 700, and 800 °C.

Phase compositions of obtained nanoparticles were studied by X-ray phase analysis using the modernized DRON-3M diffractometer. Crystal structure parameters (unit cell dimensions, positional and displacement parameters of atoms) of both series of the materials were derived by full profile Rietveld refinement by using the WinCSD program package for structural analysis [26].

The micro-Raman spectra of LN-LT nanopowders were registered by confocal Raman microscope spectrometer MonoVista CRS+. The laser beam ($\lambda = 532$ nm) was focused in a 1 mm spot on the surface of pressured nanopowder.

Temperature dependencies of electrical conductivity in the range from 300 to 820 °C were obtained via impedance measurements in the frequency range from 1 Hz to 1 MHz using impedance gain-phase analyzer (Solartron 1260, Ametek Scientific Instruments, Hampshire, UK). For this experiment, pressed pellets with thickness varying from 1.25 to 1.7 mm and diameter of 10 mm were formed from $\text{LiNb}_x\text{Ta}_{1-x}\text{O}_3$ nanopowders with $x = 0, 0.25, 0.5, 0.75,$ and 1. Throughout the preparation process, the samples were heated up to 210 °C at the rate of 2 °C/min, while the pressure applied was 190 MPa at all times. Additionally, a constant voltage of 1 kV has been applied to the samples with an intention to electrically polarize them. The so-obtained pellets were subsequently annealed in air at 600 °C for 6 h. Platinum electrodes (5 mm in diameter) were deposited on both sides of each sample via screen printing (print ink: Ferro Corporation, No. 6412 0410). The samples were subsequently thermally treated for 1 h at 800 °C to ensure electrode adhesion.

Scanning electron microscopy (SEM) imaging of $\text{LiNb}_{0.5}\text{Ta}_{0.5}\text{O}_3$ sample has been performed after initial annealing at 600 °C (Figure 3) and after impedance measurements (Figure 4). The comparison of these two images reveals an increase in average grain size from approximately 100 to 200 nm due to temperature treatment during electrode preparation and the impedance studies. The SEM analysis after the impedance spectroscopy experiment, performed on a larger fragment of the sample, also demonstrates a high homogeneity of grain size distribution along the area.

Obtained impedance spectra of $\text{LiNb}_x\text{Ta}_{1-x}\text{O}_3$ pressed samples are represented in form of Nyquist diagrams. Subsequently, an electrical equivalent-circuit model consisting of a constant phase element (CPE) connected in parallel with a bulk resistance R_B is fitted to the measured data. The intercepts of semicircles in the range of low frequencies are interpreted as samples resistance and subsequently converted to conductivity using the relation $\sigma = t(A \times R_B)^{-1}$, where t and A are the thickness of the sample and the electrode area, respectively.

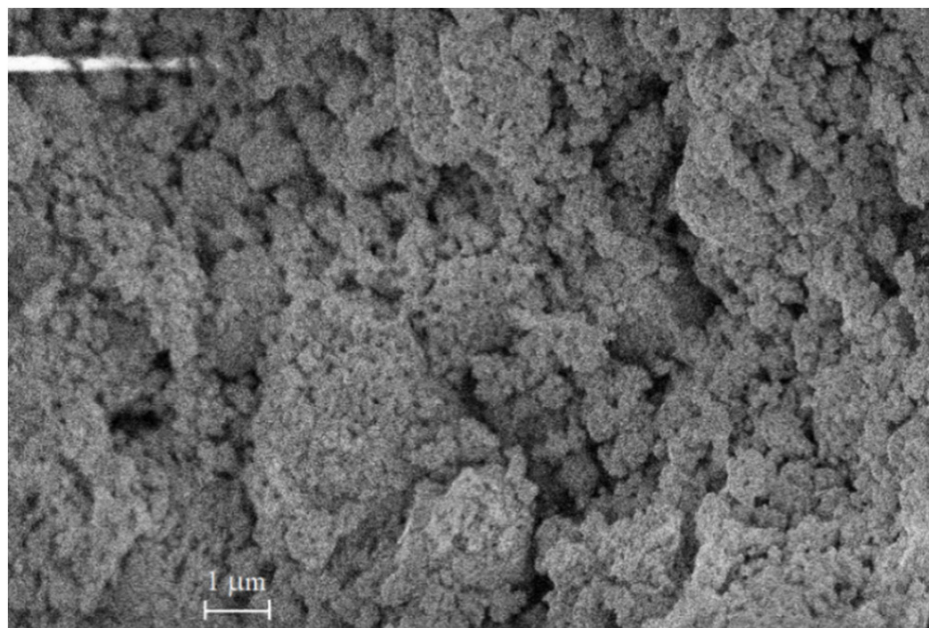


Figure 3. Scanning electron microscopy image of pressed LiNb_{0.5}Ta_{0.5}O₃ after initial annealing at 600 °C.

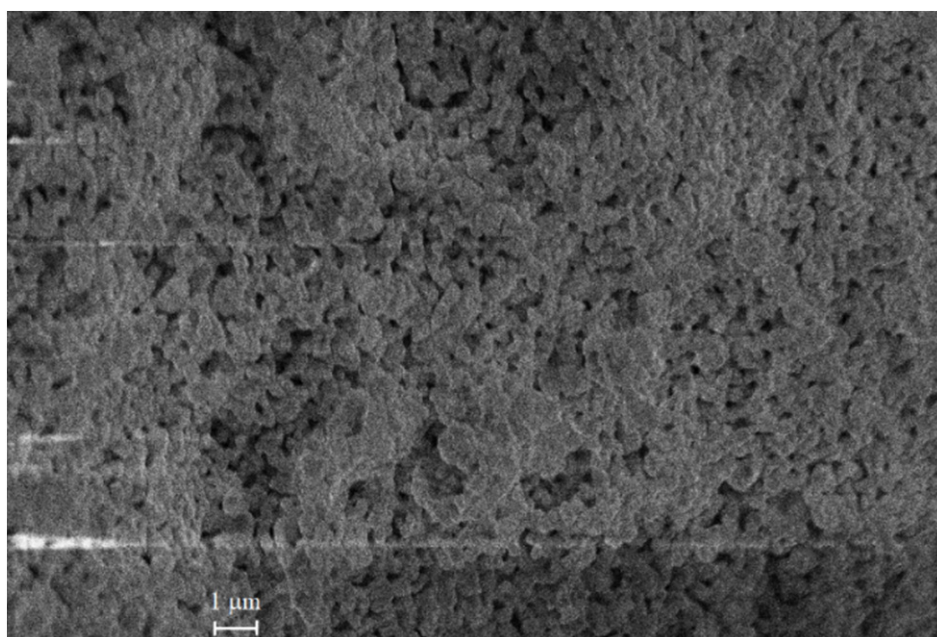


Figure 4. Scanning electron microscopy image of pressed LiNb_{0.5}Ta_{0.5}O₃ after impedance measurements performed at 820 °C.

3. Results and Discussion

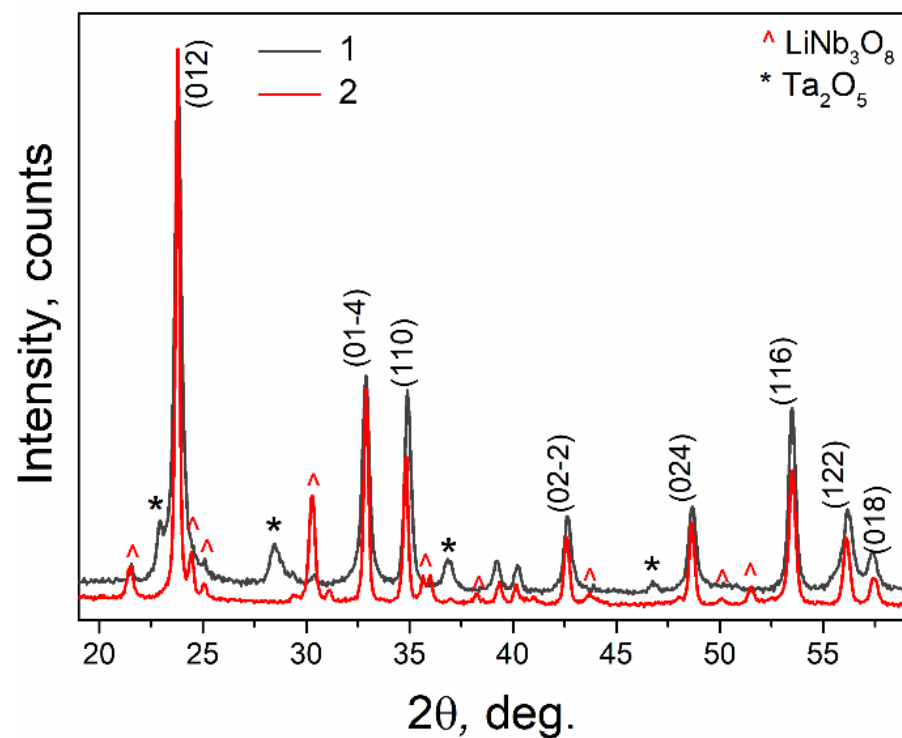
3.1. X-ray Diffraction

X-ray diffraction (XRD) study of all the LiNb_{1-x}Ta_xO₃ samples annealed at 550 °C revealed a rhombohedral LiNbO₃-type structure as the main phase with some amount of the parasitic phase Li(Nb,Ta)₃O₈, and unreacted Ta₂O₅ and Nb₂O₅ (Table 2). Only the sample with $x = 0$ that corresponds to the ‘pure’ LiNbO₃ shows single phase composition as in work [21].

Table 2. Lattice parameters (a , c), average grain size, and microstrains values ($\langle \varepsilon \rangle$) of two $\text{LiNb}_{1-x}\text{Ta}_x\text{O}_3$ series heat treated at 550 and 800 °C.

Sample	x	T , °C	Parasitic Phases	a , Å	c , Å	D_{ave} , nm	$\langle \varepsilon \rangle$, %
S01	0	550	–	5.1483(3)	13.8484(9)	41	0.088
		800	–	5.1517(2)	13.8335(7)	206	0.108
S02	0.25	550	$\text{Li}(\text{Nb},\text{Ta})_3\text{O}_8$	5.1477(3)	13.822(1)	50	0.143
		800	$\text{Li}(\text{Nb},\text{Ta})_3\text{O}_8$	5.1521(3)	13.8148(8)	171	0.105
S03	0.5	550	$\text{Ta}_2\text{O}_5 + \text{LiNb}_3\text{O}_8$	5.1534(4)	13.808(1)	63	0.107
		800	$\text{Li}(\text{Nb},\text{Ta})_3\text{O}_8$	5.153(1)	13.778(3)	97	0.128
S04	0.75	550	Ta_2O_5	5.149(2)	13.788(5)	31	0.093
		800	$\text{Li}(\text{Nb},\text{Ta})_3\text{O}_8$	5.1558(7)	13.753(2)	92	0.139
S05	1	550	Ta_2O_5	5.1529(6)	13.767(2)	66	0.114
		800	$\text{Li}(\text{Nb},\text{Ta})_3\text{O}_8$	5.1593(4)	13.745(2)	80	0.135

Observable broadening of the Bragg's peaks on the nanocrystalline character for the powders was revealed. Additional heat treatment of the materials at 800 °C led to the narrowing of the diffraction peaks and to the considerable change of the phase composition of the $\text{LiNb}_{1-x}\text{Ta}_x\text{O}_3$ samples with x from 0.5 to 1, in which the increase of monoclinic LiNb_3O_8 or $\text{Li}(\text{Nb},\text{Ta})_3\text{O}_8$ phases and disappearing of individual Ta_2O_5 and Nb_2O_5 oxides were detected (see, e.g., Figure 5). No significant changes of the phase composition in the samples with $x = 0$ and 0.25 were observed after such annealing of the samples.

**Figure 5.** XRD patterns of the “S04” sample with a nominal composition $\text{LiNb}_{0.25}\text{Ta}_{0.75}\text{O}_3$ heat treated at 550 °C and 800 °C. For the main rhombohedral LN-LT phase, the Miller's indices are given (1—S04 at 550 °C; 2—S04 at 800 °C).

As an example, Figure 6 demonstrates graphical results of Rietveld refinement of $\text{LiNb}_{0.75}\text{Ta}_{0.25}\text{O}_3$ material heat treated at 800 °C.

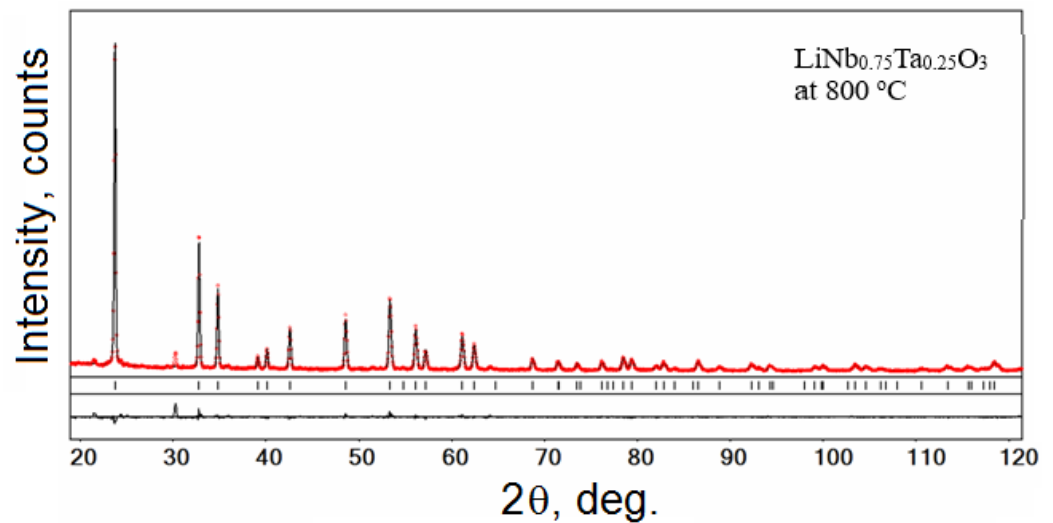


Figure 6. Results of Rietveld refinement of the $\text{LiNb}_{0.75}\text{Ta}_{0.25}\text{O}_3$ material heat treated at 800 °C. An experimental XRD pattern (dots) is shown in comparison with the calculated pattern. The difference between measured and calculated profiles is shown as a curve below the diagram. Short vertical bars indicate the positions of diffraction maxima in space group $R3c$.

The WinCSD programme package was also used for the evaluation of microstructural parameters of the powders, as presented in Table 1. The average grain size and microstrains $\langle \varepsilon \rangle = \langle \Delta d \rangle / d$ associated with the dispersion of interplanar distances d were derived from the analysis of angular dependence of the Bragg's peaks profiles. For the correction of instrumental broadening, the LaB_6 external standard was used. It was revealed that the average grain size of the $\text{LiNb}_{1-x}\text{Ta}_x\text{O}_3$ powders annealed at 550 °C is between 31 and 66 nm. Increase of thermal annealing temperature led to essential growth of grain size, being especially pronounced for the nominally pure LiNbO_3 and $\text{LiNb}_{0.75}\text{Ta}_{0.25}\text{O}_3$ sample. Corresponding changes for tantalum-rich materials are much less pronounced: the average grain size of $\text{LiNb}_{1-x}\text{Ta}_x\text{O}_3$ at 800 °C powders with x from 0.5 to 1 lies between 80 and 97 nm (see Table 2).

Analysis of the obtained structural parameters revealed that an increase of Ta content in both of the $\text{LiNb}_{1-x}\text{Ta}_x\text{O}_3$ specimens treated at 550 and 800 °C leads to the increase of the a -parameter and simultaneous decrease of the c -parameter (Figure 7a). As a result, a significant decrease of the c/a ratio and minor decrease of the unit cell volume in both $\text{LiNb}_{1-x}\text{Ta}_x\text{O}_3$ series is observed. It is observed that similar to the compositional effect on the unit cell dimensions of $\text{LiNb}_{1-x}\text{Ta}_x\text{O}_3$ materials, there is an increase of the heat treatment temperature from 550 to 800 °C, which led to increase of the a -parameter and simultaneous reduction of the c -parameter (see Figure 7).

The comparison of the obtained structural parameters of LN-LT samples with the corresponding structural data for nominally pure LN and LT [27–33] points to the formation of the continuous $\text{LiNb}_{1-x}\text{Ta}_x\text{O}_3$ solid solution.

As can be seen from the results presented in Table 2 and Figure 7, after annealing at $T = 550$ °C, the phase analysis indicates that niobium and/or tantalum oxides prevail among the traces of parasitic phases in the resulting nanopowders with the lithium niobate structure. At the same time, after annealing at $T = 800$ °C, the predominant parasitic phase is the compound $\text{Li}(\text{Nb,Ta})_3\text{O}_8$, which, as compared to $\text{Li}(\text{Nb,Ta})\text{O}_3$, contains less lithium. The latter is due to the sublimation of lithium in the form of oxide [34]. This result indicates that the optimal annealing temperature of nanopowders lies in the range of 550–800 °C. In order to optimize the heat treatment conditions for obtaining single-phase

nanocrystalline powders, a number of experiments were carried out on the milling and annealing of equiatomic lithium niobate–tantalate $\text{LiNb}_{0.5}\text{Ta}_{0.5}\text{O}_3$ at different milling times and different annealing temperatures.

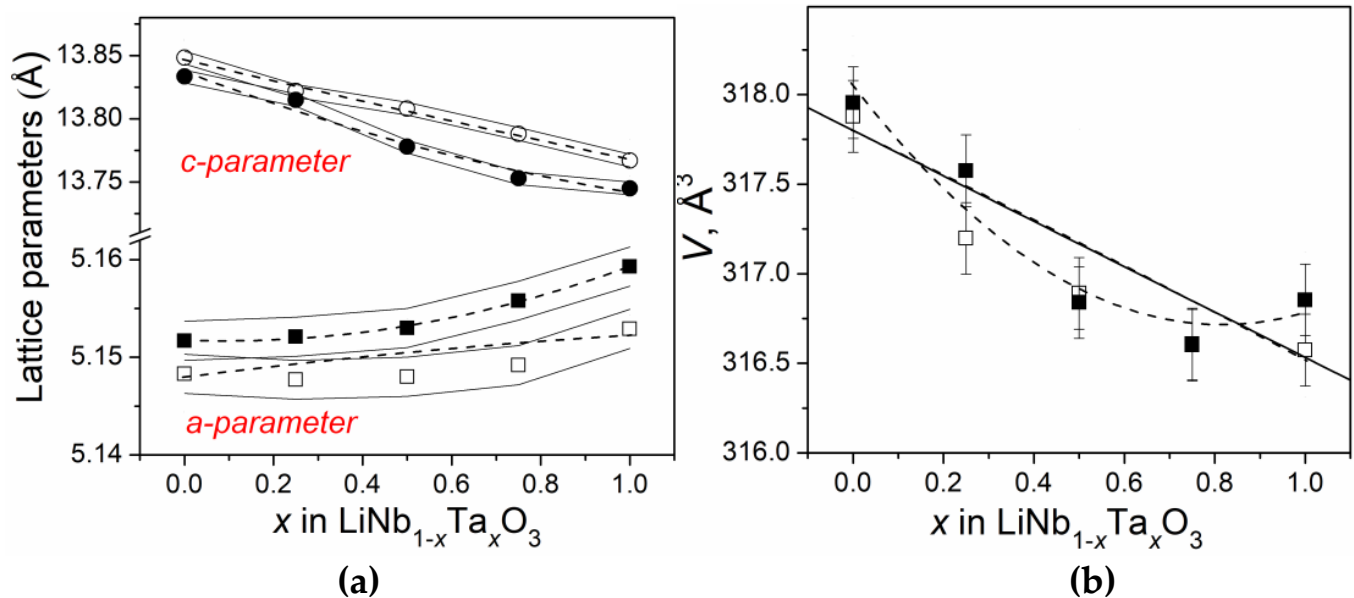


Figure 7. Concentration dependence of the lattice parameters (a) and unit cell volume (b) in $\text{LiNb}_{1-x}\text{Ta}_x\text{O}_3$ at 550 °C and $\text{LiNb}_{1-x}\text{Ta}_x\text{O}_3$ at 800 °C series. The dashed lines are a guide for eyes (empty symbols—samples annealed at 550 °C; solid symbols—samples annealed at 800 °C).

Based on the data of X-ray phase analysis of the synthesized compounds, it was found that the best results were achieved with a milling time of 12–15 h and a heat treatment temperature of 650–700 °C for 5 h. Such modes ensure the absence of parasitic phases (within the accuracy of the measurement method) and the absence of violation of stoichiometric ratio Li/Nb. Diffraction patterns of powders obtained in optimal conditions are shown in Figure 8.

3.2. Raman Spectra

The micro-Raman spectra of LN-LT nanopowders with different Nb and Ta content, annealed at 550 °C, are shown in Figure 9, and the positions of the observed bands are indicated in Table 3. As it is seen from Figure 9, the Raman spectra of LN-LT with different x are generally similar; however, some peculiarities are observed. Particularly, in the spectrum of pure LN, 15 Raman bands can be distinguished, 11 of which can be attributed to A1 and E vibrational modes. The A1 modes are polarized along the Z-axis, while the doubly degenerate E modes correspond to ionic motions along the X or Y-axis [35,36]. In the spectrum of LN-LT ($x = 0.25$), 25 Raman bands can be distinguished; for $x = 0.5$, the number of bands is equal to 20, for $x = 0.75$ to 15 and for pure LT to 17 (see Table 3). The differences in the number of distinguished bands could probably be caused by the overlapping of some bands with those with higher intensity. The observed differences are associated with different compositions of the nanopowders as well as with probably non-optimal technology regimes of nanopowders synthesis. Particularly, the following main specific features of the LN-LT nanopowders Raman spectra were revealed.

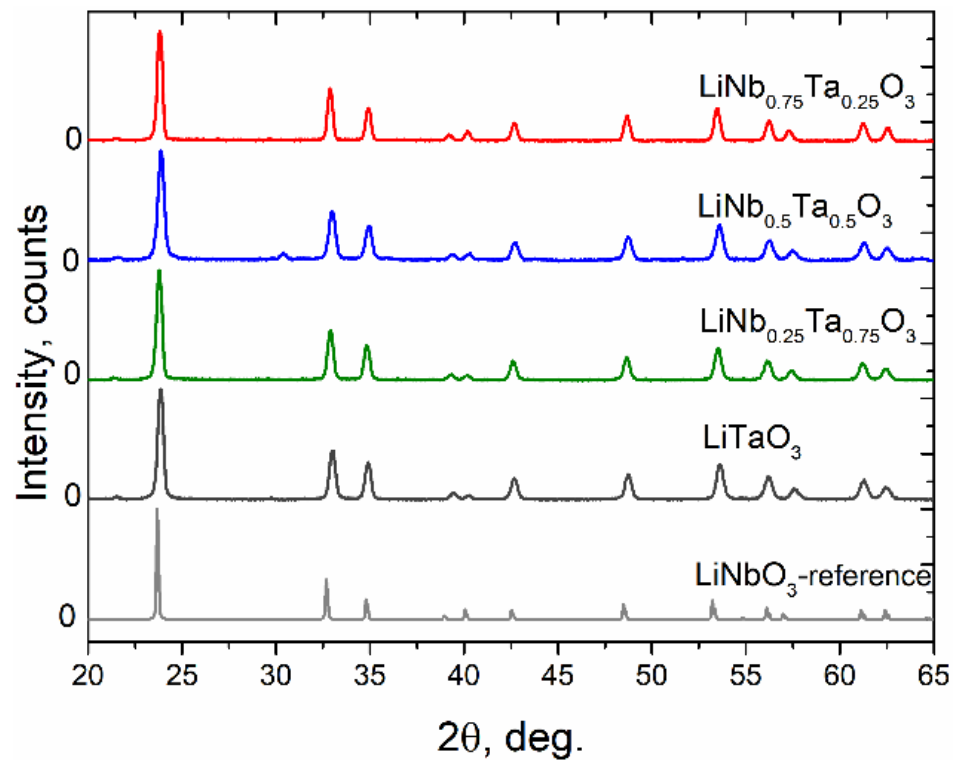


Figure 8. Diffraction patterns of $\text{LiNb}_{1-x}\text{Ta}_x\text{O}_3$ nanopowders ($x = 0.25; 0.5; 0.75; 1$) obtained by mechano-synthesis in optimal modes (milling speed—600 rpm, milling time—15 h, annealing at 700°C for 5 h), as well as the reference diffractogram of LiNbO_3 .

1. Few low-frequency bands near $73\text{--}75$ and $90\text{--}97\text{ cm}^{-1}$ are observed for the nanopowders with $x \neq 0$. These bands cannot be linked with known Raman bands of LT [35–37]. In accordance with the results of [38], these bands could be induced by the presence of $\text{Li}(\text{Nb,Ta})_3\text{O}_8$ phase, as identified by X-ray diffraction technique (see Table 2).
2. A more intensive band near $117\text{--}125\text{ cm}^{-1}$ is observed only for the LN-LT sample with $x = 0.5$. The presence of this band could be attributed to the contribution of $\text{Li}(\text{Nb,Ta})_3\text{O}_8$ and Ta_2O_5 additional phases in this sample. Note that the authors in [38] observed the close bands at 116 and 136 cm^{-1} and attributed them to LiNb_3O_8 . The bands near 100 cm^{-1} were attributed to Ta_2O_5 by the authors of [39]. As it is followed from the XRD data (see Table 1), the simultaneous presence of $\text{Li}(\text{Nb,Ta})_3\text{O}_8$ and Ta_2O_5 phases occurs only in the sample with $x = 0.5$, so the overlay of corresponding bands can result in a peculiar form of its spectrum. Furthermore, the sample with $x = 0.5$, i.e., with the composition intermediate between pure LN and pure LT, ought to essentially reveal the bands of both crystals, so it is no wonder that the spectrum of this sample has the most complex character. Furthermore, the sample with $x = 0.5$ reveals a significant increase of the bands' intensities near 260 and $630\text{--}670\text{ cm}^{-1}$ that visually looks like a widening of intensive neighboring peaks. This result is in good agreement with [40], where two intensive neighboring bands in the region of 600 cm^{-1} were also observed for the LN-LT sample with $x = 0.553$. Finally, it should be noted that the bands near 600 cm^{-1} are considerably broad for all investigated samples in comparison with the other observed bands. This is consistent with the results in [41] where it is concluded that the band at 600 cm^{-1} is broader for non-poled LN samples (particularly, nanopowders) than for polarized.
3. The Raman spectra of LN and LT nano- and micropowders are shown in Figure 10 for comparison purposes. The latter were obtained by the crushing of LN and LT single crystals grown at SRC 'Electron-Carat'. As seen from Figure 10, the band observed at about $1008\text{--}1009\text{ cm}^{-1}$ for LT nanopowder is not pronounced for LT

micropowder as well as for LN compounds. The similar band can be observed in Figure 9 for nanopowders with $x \neq 0$. As it is seen from Figure 9, the intensity of this band increases with increasing of x . Moreover, for $x = 0.5$, this band splits into two with the frequencies of 994 and 1008 cm^{-1} . As it is shown in [39], this band is absent in Ta_2O_5 Raman spectrum. Since the data about Raman scattering in LiNb_3O_8 are not available in this spectral range, we cannot exclude that this band is linked with the LiNb_3O_8 (or LiTa_3O_8) phase. However, as it is seen from Table 2, the LiTa_3O_8 phase is absent in the pure LT sample annealed at 550 $^\circ\text{C}$ as well as in the sample with $x = 0.75$ (within the limits of accuracy). Thus, we have to conclude that the nature of this band cannot be clearly determined from current experiments and requires additional studies.

4. Contrary to the results in [42], we did not observe any remarkable effect of grain size reduction, i.e., decreasing of the intensities of all Raman bands caused by grain size decrease (see Figure 10).
5. Increasing the spectral range up to 4000 cm^{-1} allows revealing the weak vibrations at 1600 and 3400 cm^{-1} (looking as low-intensive wide bands) that can be caused by the traces of OH^- groups, which are always present in LN and LT as well as the traces of HCO_3^- groups (near 1750 and 2900 cm^{-1}) present in synthesized compounds, which is probably due to the use of lithium carbonate as a component of the initial mixture.

Similarly to X-ray studies, we have measured the Raman spectra of nanopowder samples obtained under optimal conditions. These spectra are shown in Figure 11.

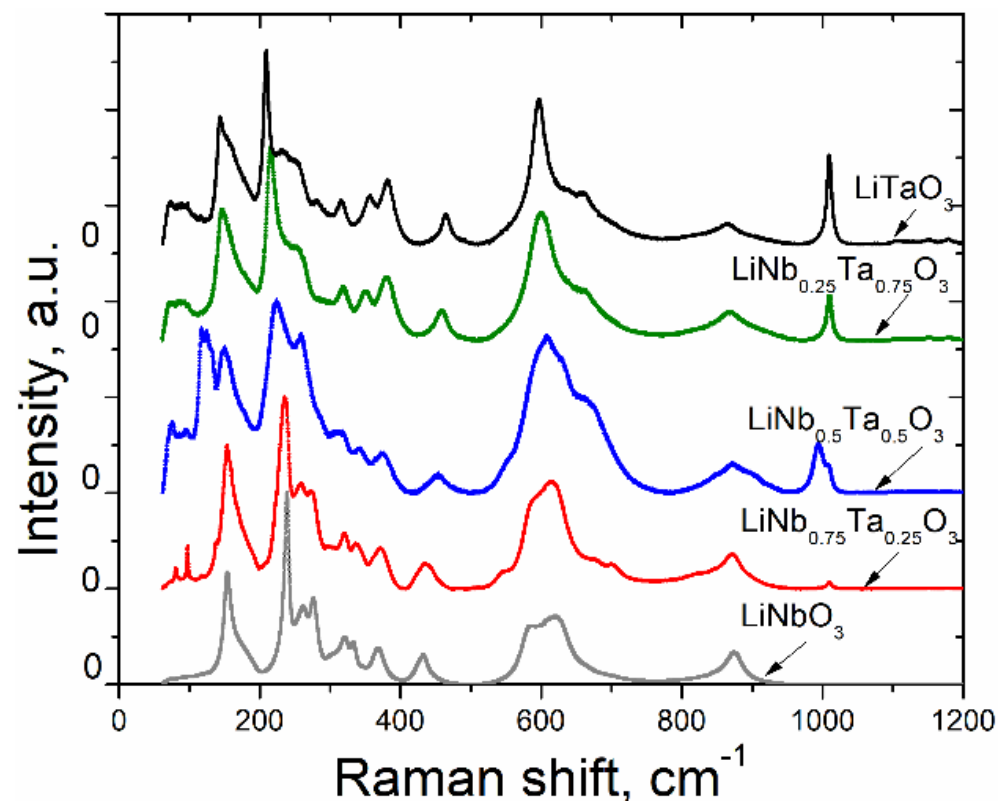


Figure 9. Raman spectra of $\text{LiNb}_{1-x}\text{Ta}_x\text{O}_3$ nanopowders obtained in non-optimal synthesis conditions.

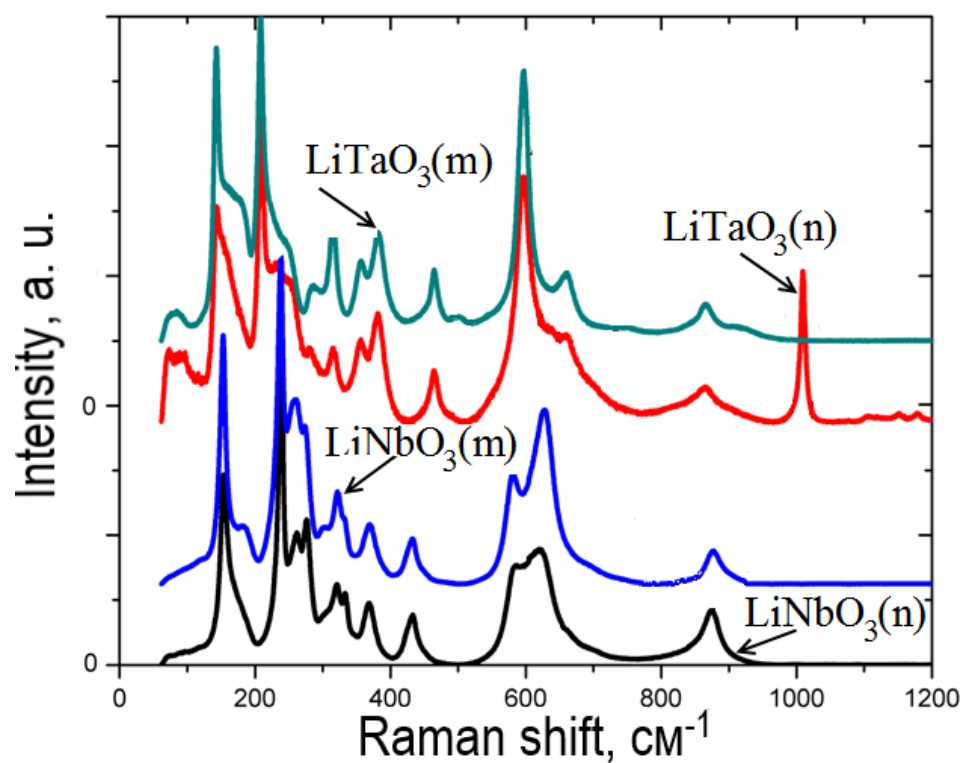


Figure 10. Raman spectra of nanopowders (n) of LiNbO_3 and LiTaO_3 synthesized by mechanochemical treatment and the ones of micropowders (m) of LiNbO_3 and LiTaO_3 obtained by crushing.

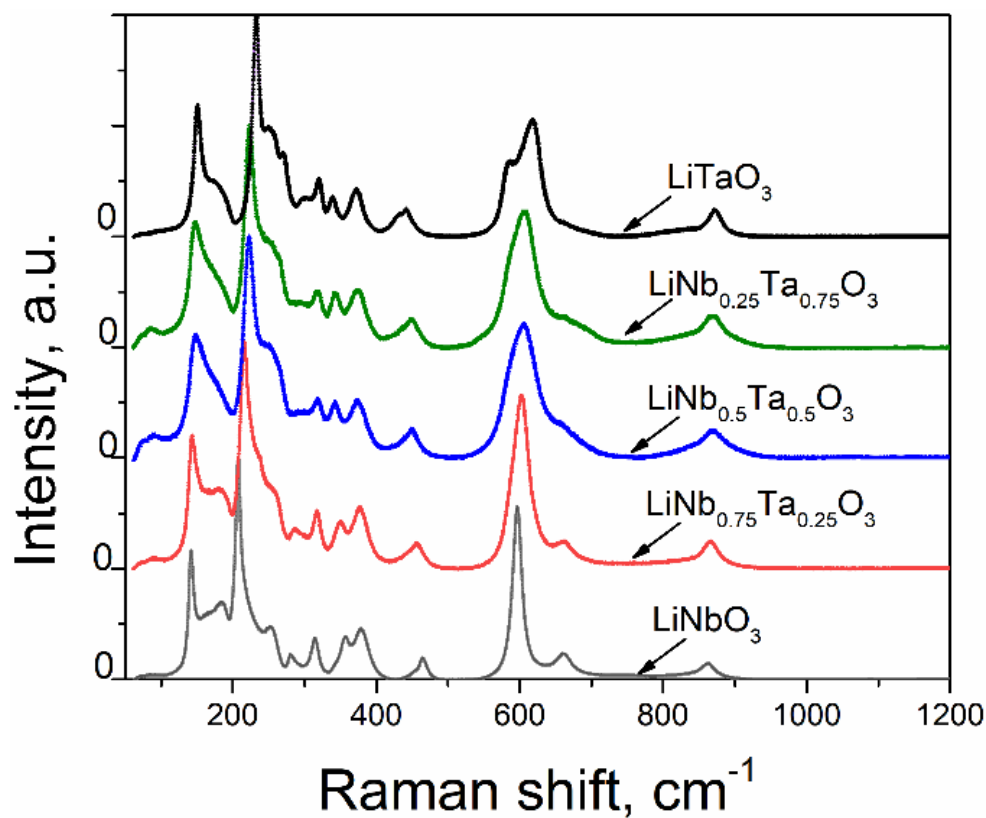


Figure 11. Raman spectra of $\text{LiNb}_{1-x}\text{Ta}_x\text{O}_3$ nanopowders obtained in optimal synthesis conditions.

Table 3. The observed bands in Raman spectra of $\text{LiNb}_{1-x}\text{Ta}_x\text{O}_3$ nanopowders.

$x = 0$		$x = 0.25$		$x = 0.5$		$x = 0.75$		$x = 1$	
Raman Shift, cm^{-1}	Intensity, a. u.	Raman Shift, cm^{-1}	Intensity, a. u.	Raman Shift, cm^{-1}	Intensity, a. u.	Raman Shift, cm^{-1}	Intensity, a. u.	Raman Shift, cm^{-1}	Intensity, a. u.
117.3	556	63.5	151	75.5	3779	73.8	2037	73.1	2275
153.8	5873	73.2	391	95.8	3327	90.2	2046	97	2194
180	1089	80.8	1117	117.1	8657	146.9	6845	143.2	6681
238.8	10,002	97.5	2255	124.2	8534	168.4	4115	162	4985
262.6	4068	117.7	715	131	7601	215.3	10,093	209.1	10,133
276.7	4481	138	2445	150.2	7676	240.2	5079	232.5	4917
303	1582	153.8	7500	224.3	10,117	252.7	4891	250.5	4384
321	2491	168.8	4176	258.3	8375	319	2778	280.8	2294
333	2220	208.6	1390	312.4	3266	351.1	2550	316	2327
369	1904	235.9	9978	342.3	2388	380.5	3293	356.2	2579
432.8	1550	259	5508	375.7	2129	458.3	1570	381.5	3387
584.6	3074	272.7	5113	453.1	997	600.1	6663	465.1	1618
621.3	3557	298.6	2242	608.4	8264	660.7	2598	597	7575
700.8	464	320.8	2914	629.7	7113	868.2	1535	637	2886
875	1681	336.4	2391	664.1	4978	1009.7	2344	660.2	2741
		371.7	2150	849.6	1035			865.8	1122
		436	1339	872.9	1571			1009.2	4684
		547.3	945	906	954				
		597.7	5018	994.1	2675				
		615.5	5608	1008.1	1536				
		676	1572						
		700	1300						
		821.8	808						
		872	1841						
		1009.7	341						

As seen from Figure 11, the spectra for the $\text{LiNb}_{1-x}\text{Ta}_x\text{O}_3$ are generally consistent with those recorded for samples, which were obtained in non-optimal conditions (see also Figure 9). The only difference is the band observed near 1000 cm^{-1} for the $\text{LiNb}_{1-x}\text{Ta}_x\text{O}_3$ specimens with $x = 0.25, 0.5, 0.75,$ and 1 , obtained in a non-optimal regime (Figure 9). This band vanishes from the spectra of specimens, which are obtained in optimal regimes. The nature of this band remains not clear and requires additional studies.

3.3. Electrical Conductivity

Impedance data of the pressed $\text{LiNb}_x\text{Ta}_{1-x}\text{O}_3$ samples are exemplarily shown for $400 \text{ }^\circ\text{C}$ (Figure 12) and $600 \text{ }^\circ\text{C}$ (Figure 13) in the form of Nyquist diagrams. The representation of the resistivity is chosen to eliminate the geometrical factors of the samples (thickness and area). At $400 \text{ }^\circ\text{C}$, the impedance data of all samples show a slightly depressed single arc semicircle. Such depression could be attributed to the non-ideal capacitance of the samples, which corresponds to low values of the CPE exponents obtained from fitting of an R_b -CPE equivalent circuit model to experimental data. In particular, at $400 \text{ }^\circ\text{C}$, exponent values vary between 0.74 (LiTaO_3) and 0.85 ($\text{LiNb}_{0.75}\text{Ta}_{0.25}\text{O}_3$) and slightly decrease with the tempera-

ture increase. Another possible interpretation implies that the obtained impedance spectra may consist of two overlapping semicircles, with similar relaxation times, representing grain interior and grain boundary conduction mechanisms, respectively [43]. We note that in case of nanostructured materials, the grain boundary contributions may significantly overlap with that of the grain interiors, making it hard to distinguish between them [43,44].

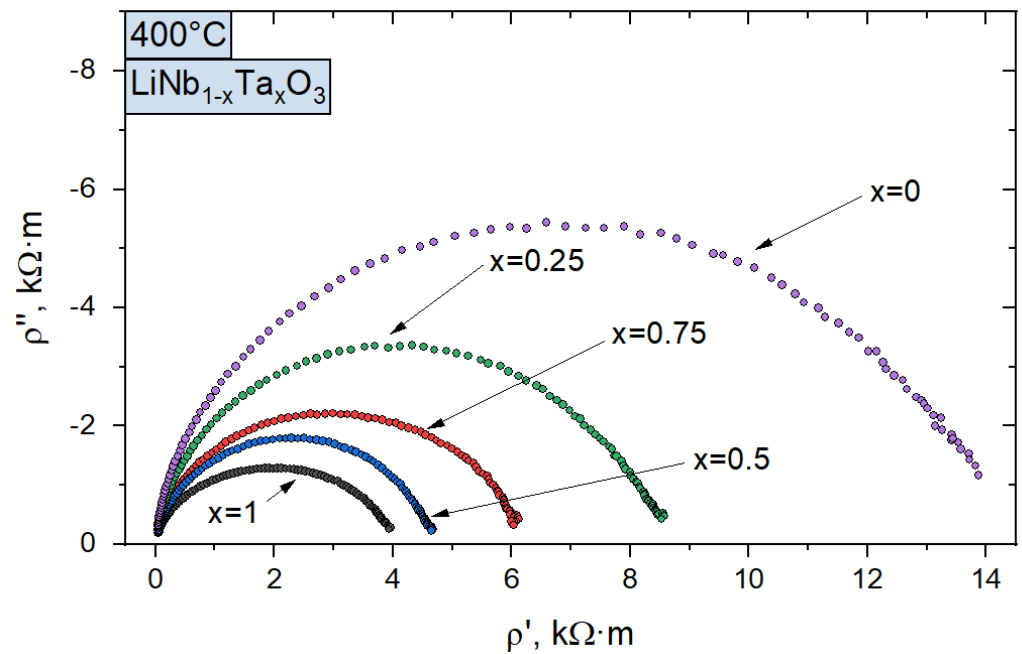


Figure 12. Complex impedance of pressed $\text{LiNb}_{1-x}\text{Ta}_x\text{O}_3$ samples measured at 400 °C.

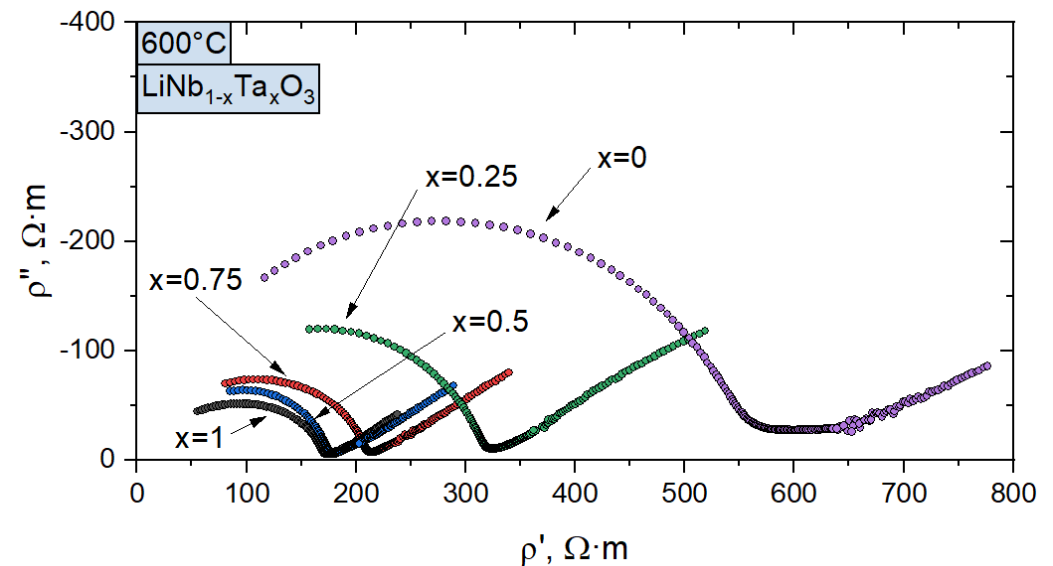


Figure 13. Complex impedance of the pressed $\text{LiNb}_{1-x}\text{Ta}_x\text{O}_3$ samples measured at 600 °C.

Impedance spectra of all samples at temperatures above 500 °C reveal the existence of linear region of $\rho''(\rho')$ dependence, which follows the semicircle intercept at lower frequencies. This is exemplarily shown in Nyquist diagram at 600 °C (Figure 13). At this temperature, the impedance of the samples has been additionally measured down to 0.01 Hz in order to examine the low-frequency region of the $\rho''(\rho')$ dependence in more detail; however, no changes in the line slope were observed. According to [45], such peculiarity at low frequencies can be attributed to the electrode effect, which is typical for

an ionic conductor: mobile charge carriers in form of ions are blocking the metal–sample interface. On the other hand, a similar behavior of $Z''(Z')$ dependence at low frequencies, which was observed in [46] for polycrystalline lithium niobate samples at temperatures above 550 °C, was associated with a grain boundaries conduction mechanism.

The temperature dependencies of $\text{LiNb}_x\text{Ta}_{1-x}\text{O}_3$ conductivity are shown in Figure 14 in form of Arrhenius plots. Generally, the behavior of conductivity is similar to that of single crystalline $\text{LiNb}_x\text{Ta}_{1-x}\text{O}_3$ reported in [47]. Furthermore, the conductivity tends to correlate with Nb/Ta ratio, increasing with an increase of Ta content and reaching the values at 820 °C of 0.022 S/m and 0.076 S/m for $x = 0$ and $x = 1$, respectively. However, the conductivity of $\text{LiNb}_x\text{Ta}_{1-x}\text{O}_3$ specimen with $x = 0.5$ deviates from this correlation, which could not be solely attributed to experiment uncertainty. The latter, according to our estimations, is approximately 6% at 800 °C. This issue requires additional studies and will be a subject of subsequent investigations.

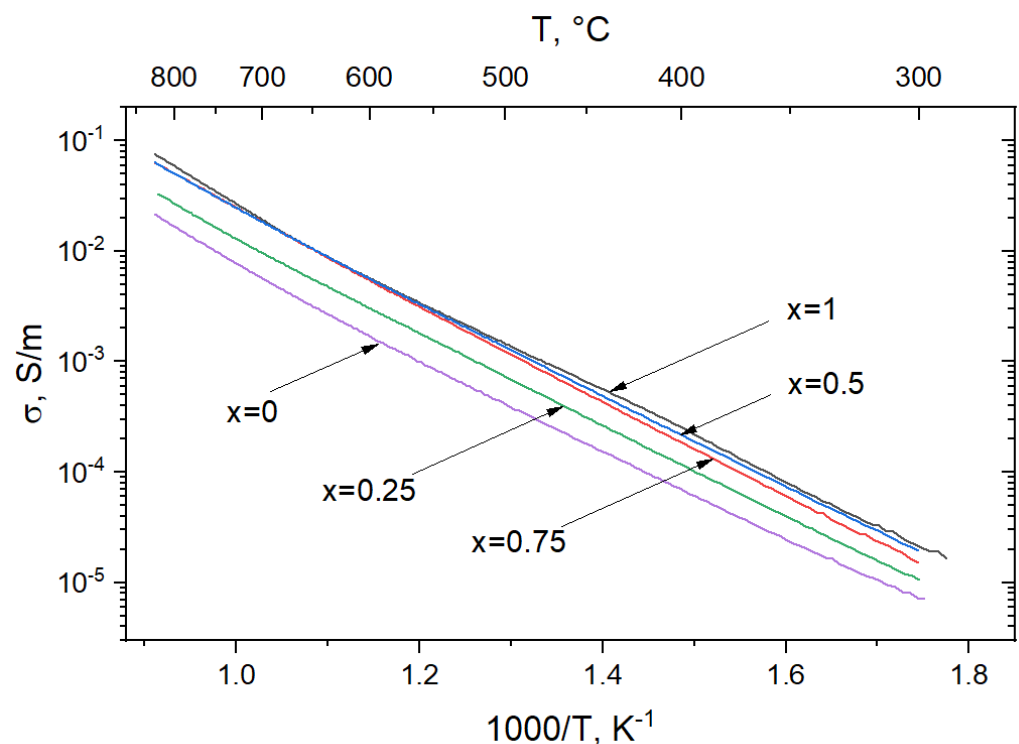


Figure 14. Temperature dependence of conductivity of $\text{LiNb}_{1-x}\text{Ta}_x\text{O}_3$ pressed pellets.

The absolute values of conductivity (Figure 14) are generally higher, comparing to the obtained previously for single crystalline and polycrystalline LiNbO_3 and LiTaO_3 [45–52]. As reported in [51], such a difference is associated with a greater number of free ions in polycrystalline LiNbO_3 and LiTaO_3 due to a developed system of grain boundaries and much more defective structure in general [51]. Consequently, the variation of conductivity, reported for different polycrystalline samples, can be attributed to differences in the average grain size in particular.

The conductivity of all samples increases linearly in Arrhenius presentation up to around 620 °C. After a transition temperature range of 620–670 °C, we observed the conductivity increase as linear again; however, the slope changes (see mark in Figure 14). This indicates that the conductivity is governed by a different process than that at lower temperatures. The obtained results enable the determination of activation energy, E_A using the relation:

$$\sigma = \frac{\sigma_0}{T} e^{-\frac{E_A}{kT}} \quad (3)$$

where σ_0 , T , E_A , and k represent the pre-exponential constant, absolute temperature, activation energy, and the Boltzmann constant, respectively. Activation energies and pre-exponential factors, obtained by fitting the Arrhenius equation to the measured conductivity data, as well as the temperature ranges for fitting are summarized in Table 4. The corresponding fits for low and high-temperature regions are exemplarily shown for the LiTaO₃ specimen in Figure 15.

Table 4. Activation energies E_A and pre-exponential coefficients σ_0 for conductivity of LiNb_{1-x}Ta_xO₃ pressed pellets at different temperatures.

Composition	300 ÷ 620 °C		670 ÷ 820 °C	
	E_A , eV	$\sigma_0 \cdot 10^6$ S/m	E_A , eV	$\sigma_0 \cdot 10^6$ S/m
LiNbO ₃	0.88 ± 0.031	0.17	1.05 ± 0.071	1.54
LiNb _{0.75} Ta _{0.25} O ₃	0.88 ± 0.011	0.32	1.01 ± 0.073	1.59
LiNb _{0.5} Ta _{0.5} O ₃	0.88 ± 0.015	0.58	1 ± 0.07	2.61
LiNb _{0.25} Ta _{0.75} O ₃	0.91 ± 0.015	0.83	0.99 ± 0.069	2.58
LiTaO ₃	0.86 ± 0.015	0.48	1.09 ± 0.072	8.33

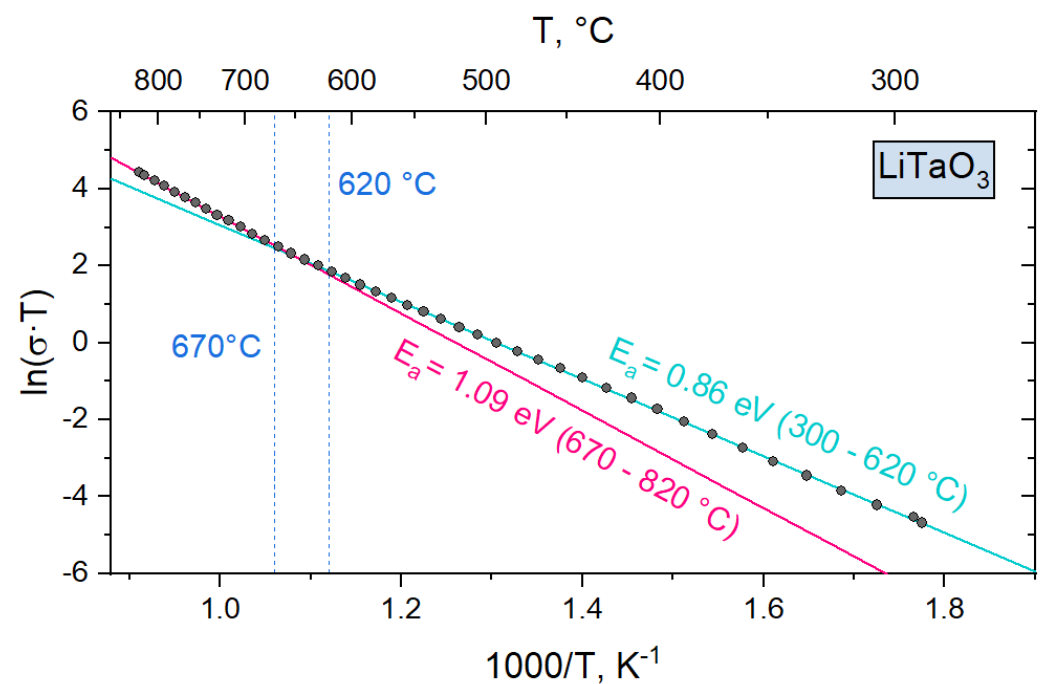


Figure 15. $\ln(\sigma \cdot T)$ vs. $1000/T$ dependence of LiTaO₃ samples (dots) and linear fits of its separate regions (lines).

Generally, the activation energies obtained in our study (Table 4) are consistent with the values obtained previously for polycrystalline lithium niobate and/or lithium tantalate [43,46,50–53], varying from 0.63 to 1.25 eV. It should be noted that the wide range of activation energies reported [43,46,50–53] is associated with their strong dependence on samples grain size, which is in particular shown in a comparative impedance spectroscopy study of single-, micro-, nanocrystalline, and amorphous lithium niobate [43]. Similar to our study, the authors in [43] observed slightly depressed semicircles on $\rho''(\rho')$ dependence of nanocrystalline LiNbO₃ and attributed such depression to the superposition of two conduction mechanisms, arising from the grain interior and grain boundary, respectively. The nanopowders studied in [43] were obtained by high-energy ball milling with the grains size of about 20 nm.

Qualitatively similar dependencies were observed for polycrystalline samples of non-stoichiometric LiNbO_3 in [53]. Here, the authors have obtained the LiNbO_3 micropowders by the ball milling technique with the grain sizes varying from 2 to 3 μm . Obtained powders were subsequently annealed and isostatically pressed in pellets at 2500 bars [53]. It is assumed in [53] that the conductivity of LiNbO_3 in low and high-temperature regions is governed by the polaronic and ionic conduction mechanisms, respectively. The activation energies obtained in [53] vary from 0.78 to 0.88 eV for the low-temperature region and from 1.07 to 1.20 eV for the high-temperature region, which is in good correlation with the values obtained in our study.

Furthermore, the authors in [51] studied the electrical properties of polycrystalline LiNbO_3 up to 800 K and obtained the activation energy of 0.88 eV, which is very close to the corresponding value in our work. The sol–gel method was applied for the synthesis of nanopowders. Subsequently, the powders were annealed at 1200 °C for 3 h and pressed in pellets [51]. The average grain size was between 0.2 and 2 μm . Since the measurements in [51] did not extend to higher temperatures, no evidence of a second conducting mechanism was observed.

4. Conclusions

In summary, it is shown in the current study that the mechanosynthesis is the most simple and most accessible method of lithium niobate and tantalate nanoparticles production. This method allows obtaining $\text{LiNb}_{1-x}\text{Ta}_x\text{O}_3$ nanopowders in only two stages: high-energy ball milling of the raw powders (Li_2CO_3 , Nb_2O_5 , Ta_2O_5) and subsequent annealing of the obtained precursors. Furthermore, this method allows completely excluding usually undesirable wet chemistry procedures from the technological process.

A number of $\text{LiNb}_{1-x}\text{Ta}_x\text{O}_3$ nanopowders ($x = 0, 0.25, 0.5, 0.75, 1$) is obtained by means of the mechanosynthesis technique for the first time, to the best of our knowledge.

The X-ray analysis of $\text{LiNb}_{1-x}\text{Ta}_x\text{O}_3$ nanopowders obtained at different conditions allowed for determination of the optimal parameters for milling and annealing runs: milling at 600 rpm for 12–15 h and subsequent annealing of powders in air at temperatures 650–700 °C for 5 h. This allowed obtaining single-phase $\text{LiNb}_{1-x}\text{Ta}_x\text{O}_3$ nanopowders for all the studied values of x .

The crystal structure of the samples was determined by the X-ray diffraction technique. The full-profile Rietveld refinement was used for determination of the crystal structure parameters and micro-structure parameters of $\text{LiNb}_{1-x}\text{Ta}_x\text{O}_3$ nanopowders. It is shown that the replacement of niobium by tantalum in the $\text{LiNb}_{1-x}\text{Ta}_x\text{O}_3$ structure asymmetrically influences the parameters of the unit cell: increasing the Ta content x leads to increasing the lattice parameter a and the simultaneous decreasing of parameter c accompanied by a slight decreasing of the unit cell volume. It is shown that the average size of crystallites varies from 31 nm (treatment only at 550 °C) to 206 nm (additional treatment at 800 °C) for different samples.

Raman scattering in $\text{LiNb}_{1-x}\text{Ta}_x\text{O}_3$ nanopowders ($x = 0, 0.25, 0.5, 0.75, 1$) obtained by mechanosynthesis was studied, to the best of our knowledge, for the first time. It is shown that the obtained Raman spectra are generally similar. Some features (band shifts, changes in their intensity, the formation of new bands) are attributed to the different values of x . For samples obtained in non-optimal milling and annealing runs, bands typical for the parasitic phases $\text{LiNb}(\text{Ta})_3\text{O}_8$, Nb_2O_5 , and/or Ta_2O_5 are observed in the spectra.

The measured temperature dependence of electrical conductivity in air up to 820 °C shows similar behavior for all studied $\text{LiNb}_{1-x}\text{Ta}_x\text{O}_3$ samples and tends to correlate with the Nb/Ta ratio. Two linear regions are observed in the Arrhenius presentation, which is attributed to different conductivity mechanisms. Activation energies vary from 0.86 ± 0.015 eV to 0.91 ± 0.015 eV for different compositions in the low-temperature region and from 0.99 ± 0.069 eV to 1.09 ± 0.072 eV at high temperatures.

Author Contributions: Conceptualization, D.S.; Data curation, S.H. and U.Y.; Investigation, L.V., Y.S., D.W., S.H. and Y.Z.; Methodology, V.S. and A.L.; Resources, I.I.S. and I.S.; Writing—original draft, O.B.; Writing—review and editing, A.S. and H.F. All authors have read and agreed to the published version of the manuscript.

Funding: Research grants from the Bundesministerium für Bildung und Forschung (BMBF, Federal Ministry of Education and research, FKZ: 01DK20009) and Ministry of Education and Science of Ukraine (M/48-2020) in frames of the joint German-Ukrainian project ‘Nanocrystalline piezoelectric compounds $\text{LiNb}_{1-x}\text{Ta}_x\text{O}_3$ for high-temperature applications’ supported this work. Furthermore, the work was partially supported by the Polish National Science Center (grant No. 2019/33/B/ST8/02142) and by the Deutsche Forschungsgemeinschaft (DFG, German Research Foundation, www.for5044.de; SU1261/1-1, FR1301/42-1).

Data Availability Statement: All relevant data presented in the article are stored according to institutional requirements and as such are not available online. However, all data used in this manuscript can be made available upon request to the authors.

Acknowledgments: Stepan Hurskyj and Uliana Yakhnevych acknowledge the partial support of the Ukrainian Ministry of Education and Science through the project DB/KINETYKA (No 0119U002249). The authors from Clausthal University of Technology acknowledge the support of the Energie-Forschungszentrum Niedersachsen, Goslar, Germany. The authors acknowledge support by Open Access Publishing Fund of Clausthal University of Technology.

Conflicts of Interest: The authors declare no conflict of interest.

References

- LiNbO₃ Crystal Market by Type (Acoustic Grade, Optical Grade, Others), by Application (Electro-Optical, Surface Acoustic Wave, Piezoelectric Sensors, Non-Linear Optical, Other) and Region—Global Forecasts to 2027. Available online: <https://www.reportsanddata.com/report-detail/global-linbo3-crystal-market-by-manufacturers-countries-type-and-application-forecast-to-2022> (accessed on 21 May 2021).
- Lithium Niobate Modulator Market—Global Industry Analysis, Size, Share, Growth, Trends, and Forecast. 2019–2027. Available online: <https://www.transparencymarketresearch.com/lithium-niobate-modulator-market.html> (accessed on 21 May 2021).
- Global Lithium Tantalate Crystal Market 2019–2027—Industry Analysis, Size, Share, Growth, Trends and Forecast. Available online: <https://www.prnewswire.com/news-releases/global-lithium-tantalate-crystal-market-2019--2027--industry-analysis-size-share-growth-trends-and-forecast-300980802.html> (accessed on 21 May 2021).
- Lithium Tantalate Crystal Market (Grade: Optical Grade, SAW Grade, and Others; and Application: Electro-Optical Modulators, Pyroelectric Detectors, Piezoelectric Transducers, Acoustic Wave Devices, and Others)—Global Industry Analysis, Size, Share, Growth, Trends, and Forecast. 2019–2027. Available online: <https://www.transparencymarketresearch.com/lithium-tantalate-crystal-market.html> (accessed on 21 May 2021).
- Xue, D.; Betzler, K.; Hesse, H. Dielectric properties of lithium niobate-tantalate crystals. *Solid State Commun.* **2000**, *115*, 581–585. [CrossRef]
- Wood, I.G.; Daniels, P.; Brown, R.H.; Glazer, A.M. Optical birefringence study of the ferroelectric phase transition in lithium niobate tantalate mixed crystals: $\text{LiNb}_{1-x}\text{Ta}_x\text{O}_3$. *J. Phys. Condens. Matter* **2008**, *20*, 235237. [CrossRef] [PubMed]
- Bartasyte, A.; Glazer, A.M.; Wondre, F.; Prabhakaran, D.; Thomas, P.A.; Huband, S.; Keebleand, D.S.; Margueron, S. Growth of $\text{LiNb}_{1-x}\text{Ta}_x\text{O}_3$ solid solution crystals. *Mater. Chem. Phys.* **2012**, *134*, 728–735. [CrossRef]
- Roshchupkin, D.; Emelin, E.; Plotitsyna, O.; Fahrtdinov, R.; Irzhak, D.; Karandashev, V.; Orlova, T.; Targonskaya, N.; Sakharov, S.; Mololkin, A.; et al. Single crystals of ferroelectric lithium niobate–tantalate $\text{LiNb}_{1-x}\text{Ta}_x\text{O}_3$ solid solutions for high-temperature sensor and actuator applications. *Acta Crystallogr. B* **2020**, *76*, 1071–1076. [CrossRef]
- Nashimoto, K.; Cima, M.J. Epitaxial LiNbO_3 thin films prepared by a sol-gel process. *Mat. Lett.* **1991**, *10*, 348–354. [CrossRef]
- Hirano, S.; Yogo, T.; Kikuta, K.; Morishita, T.; Ito, Y.; Hirano, S.; Yogo, T.; Kikuta, K.; Morishita, T. Preparation of potassium tantalate niobate by sol-gel method. *J. Amer. Cer. Soc.* **1992**, *75*, 1701–1704. [CrossRef]
- Ono, S.; Hirano, S. Processing of highly oriented lithium tantalate films by chemical solution deposition. *J. Mater. Res.* **2002**, *17*, 2532–2539. [CrossRef]
- Takahashi, M.; Yamauchi, K.; Yagi, T.; Nishiwaki, A.; Wakita, K.; Ohnishi, N.; Hotta, K.; Sahashi, I. Preparation and characterization of high-quality stoichiometric LiNbO_3 thick films prepared by the sol-gel method. *Thin Solid Film.* **2004**, *458*, 108–113. [CrossRef]
- Satapathy, S.; Gupta, P.K.; Srivastava, H.; Srivastava, A.K.; Wadhawan, V.K.; Varma, K.B.R.; Sathe, V.G. Effect of capping ligands on the synthesis and on the physical properties of the nanoparticles of LiTaO_3 . *J. Cryst. Growth* **2007**, *307*, 185–191. [CrossRef]
- Gou, J.; Wang, J.; Huang, Z.H.; Jiang, Y.D. Preparation of LiTaO_3 nano-crystalline films by sol-gel process. *Key Engin. Mat.* **2013**, *531–532*, 446–449. [CrossRef]
- Johann, F.; Jungk, T.; Lisinski, S.; Hoffmann, Á.; Ratke, L.; Soergel, E. Sol-gel derived ferroelectric nanoparticles investigated by piezoresponse force microscopy. *Appl. Phys. Lett.* **2009**, *95*, 202901. [CrossRef]

16. Liu, Y.G.; Hu, J.H.; Huang, Z.H.; Fang, M.H. Preparation of LiTaO₃ nanoparticles by a sol–gel route. *J. Sol. Gel. Sci. Technol.* **2011**, *58*, 664–668. [[CrossRef](#)]
17. Mathew, T.V.; Kuriakose, S. Synthesis and characterization of sodium–lithium niobate ceramic structures and their composites with biopolymers. *J. Adv. Cer.* **2013**, *2*, 11–20. [[CrossRef](#)]
18. Li, Y.-Y.; Chen, H.-L.; Chen, G.-J.; Kuo, C.-L.; Hsieh, P.-H.; Hwang, W.-S. Investigation of the defect structure of congruent and Fe-doped LiNbO₃ powders synthesized by the combustion method. *Materials* **2017**, *10*, 380. [[CrossRef](#)]
19. Gao, L.; Chen, H.; Wang, Z.; Zou, X. Solvothermal synthesis and characterization of lithium tantalate nanoparticles. *Key Eng. Mater.* **2014**, *602–603*, 19–22. [[CrossRef](#)]
20. de Figueiredo, R.S.; Messai, A.; Hernandez, A.C.; Sombra, A.S.B. Piezoelectric lithium niobate obtained by mechanical alloying. *J. Mater. Sci. Lett.* **1998**, *17*, 449–451. [[CrossRef](#)]
21. Khalameida, S.; Sydoruk, V.; Lebeda, R.; Skubiszewska-Zięba, J.; Zazhigalov, V. Preparation of nano-dispersed lithium niobate by mechanochemical route. *J. Therm. Anal. Calorim.* **2014**, *115*, 579–586. [[CrossRef](#)]
22. Fierro-Ruiz, C.D.; Sánchez-Dena, O.; Cabral-Larquier, E.M.; Elizalde-Galindo, J.T.; Farías, R. Structural and magnetic behavior of oxidized and reduced Fe doped LiNbO₃ powders. *Crystals* **2018**, *8*, 108. [[CrossRef](#)]
23. Kar, S.; Logad, S.; Choudhary, O.P.; Debnath, C.; Verma, S.; Bartwal, K.S. Preparation of lithium niobate nanoparticles by high energy ball milling and their characterization. *Univers. J. Mater. Sci.* **2013**, *1*, 18–24. [[CrossRef](#)]
24. Kocsor, L.; Péter, L.; Corradi, G.; Kis, Z.; Gubicza, J.; Kovács, L. Mechanochemical reactions of lithium niobate induced by high-energy ball-milling. *Crystals* **2019**, *9*, 334. [[CrossRef](#)]
25. Timoshevskii, A.N.; Ktalkherman, M.G.; Emel'kin, V.A.; Pozdnyakov, B.A.; Zamyatin, A.P. High-temperature decomposition of lithium carbonate at atmospheric pressure. *High. Temperature* **2008**, *46*, 414–421. [[CrossRef](#)]
26. Akselrud, L.; Grin, Y. WinCSD: Software package for crystallographic calculations (Version 4). *J. Appl. Crystallogr.* **2014**, *47*, 803–805. [[CrossRef](#)]
27. Abrahams, S.C.; Marsh, P. Defect structure dependence on composition in lithium niobate. *Acta Crystallogr. Sect. B Struct. Sci.* **1986**, *42*, 61–68. [[CrossRef](#)]
28. Ohgaki, M.; Tanaka, K.; Marumo, F. Structure refinement of lithium (I) niobium (V) trioxide, LiNbO₃, with anharmonic thermal vibration model. *Mineral. J.* **1992**, *16*, 150–160. [[CrossRef](#)]
29. Zotov, N.; Boysen, H.; Schneider, J.; Frey, F. Application of combined neutron and X-ray powder diffraction refinements to the structure of congruent lithium niobate. *Mater. Sci. Forum* **1994**, *166*, 631–636. [[CrossRef](#)]
30. Abrahams, S.C.; Reddy, J.M.; Bernstein, J.L. Ferroelectric lithium niobate. 3. Single crystal X-ray diffraction study at 24 °C. *J. Phys. Chem. Solids* **1966**, *27*, 997–1012. [[CrossRef](#)]
31. Iyi, N.; Kitamura, K.; Izumi, F.; Yamamoto, J.K.; Hayashi, T.; Asano, H.; Kimura, S. Comparative study of defect structures in lithium niobate with different compositions. *J. Solid State Chem.* **1992**, *101*, 340–352. [[CrossRef](#)]
32. Abrahams, S.C.; Bernstein, J.L. Ferroelectric lithium tantalate. 1. single crystal X-ray diffraction study at 24 °C. *J. Phys. Chem. Solids* **1967**, *28*, 1685–1692. [[CrossRef](#)]
33. Abrahams, S.C.; Hamilton, W.C.; Sequeira, A. Ferroelectric lithium tantalate. 2. Single crystal neutron diffraction study at 24 °C. *J. Phys. Chem. Solids* **1967**, *28*, 1693–1698. [[CrossRef](#)]
34. Wang, S.Y.; Jiang, H. Synthesis and Characterization of LiNbO₃ Powders by Thermal Decomposition Method at Low Temperature. *Ferroelectrics* **2011**, *413*, 212–219. [[CrossRef](#)]
35. Gorelik, V.S.; Abdurakhmonov, S.D.; Sidorov, N.V.; Palatnikov, M.N. Raman scattering in lithium niobate and lithium tantalate single crystals and ceramics. *Inorg. Mater.* **2019**, *55*, 524–532. [[CrossRef](#)]
36. Ridah, A.; Bourson, P.; Fontana, M.D.; Malovichko, G. The composition dependence of the Raman spectrum and new assignment of the phonons in LiNbO₃. *J. Phys. Cond. Matter* **1997**, *9*, 9687–9693. [[CrossRef](#)]
37. Repelin, Y.; Husson, E.; Bennani, F.; Proust, C. Raman spectroscopy of lithium niobate and lithium tantalate. Force field calculations. *J. Phys. Chem. Solids* **1999**, *60*, 819–825. [[CrossRef](#)]
38. Bartasyte, A.; Plausinaitiene, V.; Abrutis, A.; Stanionyte, S.; Margueron, S.; Boulet, P.; Kobata, T.; Uesu, Y.; Gleize, J. Identification of LiNbO₃, LiNb₃O₈ and Li₃NbO₄ phases in thin films synthesized with different deposition techniques by means of XRD and Raman spectroscopy. *J. Phys.: Condens. Matter.* **2013**, *25*, 205901. [[CrossRef](#)]
39. Verma, N.; Mari, B.; Singh, K.C.; Jindal, J.; Mollar, M.; Rana, R.; Pereira, A.L.J.; Manjón, F.J. Structural and optical properties of Ta₂O₅:Eu³⁺: Mg²⁺ or Ca²⁺ phosphor prepared by molten salt method. *AIP Conf. Proc.* **2016**, *1724*, 020082. [[CrossRef](#)]
40. Rüsing, M.; Sanna, S.; Neufeld, S.; Berth, G.; Schmidt, W.G.; Zrenner, A.; Yu, H.; Wang, Y.; Zhang, H. Vibrational properties of LiNb_{1-x}Ta_xO₃ mixed crystals. *Phys. Rev. B.* **2016**, *93*, 284305. [[CrossRef](#)]
41. Golubović, A.; Gajić, R.; Hinić, I.; Šćepanović, M. IR and Raman spectra of poled and unpoled LiNbO₃ single crystals. *J. Alloy. Comp.* **2008**, *460*, 74–78. [[CrossRef](#)]
42. Heitjans, P.; Masoud, M.; Feldhoff, M.; Wilkening, M. NMR and impedance studies of nanocrystalline and amorphous ion conductors: Lithium niobate as a model system. *Faraday Discuss.* **2007**, *134*, 67–82. [[CrossRef](#)]
43. Chen, R.H.; Chen, L.F.; Chia, C.T. Impedance spectroscopic studies on congruent LiNbO₃ single crystal. *J. Phys. Condens. Matter* **2007**, *19*, 086225. [[CrossRef](#)]
44. Huanosta, A.; West, A.R. The electrical properties of ferroelectric LiTaO₃ and its solid solutions. *J. Appl. Phys.* **1987**, *61*, 5386–5391. [[CrossRef](#)]

45. Lanfredi, S.M.; Rodrigues, A.C. Impedance spectroscopy study of the electrical conductivity and dielectric constant of polycrystalline. *J. Appl. Phys.* **1999**, *86*, 2215–2219. [[CrossRef](#)]
46. Suhak, Y.; Roshchupkin, D.; Redkin, B.; Kabir, A.; Jerliu, B.; Ganschow, S.; Fritze, H. Correlation of Electrical Properties and Acoustic Loss in Single Crystalline Lithium Niobate-Tantalate Solid Solutions at Elevated Temperatures. *Crystals* **2021**, *11*, 398. [[CrossRef](#)]
47. Rahn, J.; Huger, E.; Dorrer, L.; Ruprecht, B.; Heitjans, P.; Schmidt, H. Li self-diffusion in lithium niobate single crystals at low temperatures. *Phys. Chem. Chem. Phys.* **2012**, *14*, 2427–2433. [[CrossRef](#)] [[PubMed](#)]
48. Weidenfelder, A.; Schulz, M.; Fielitz, P.; Shi, J.; Borchardt, G.; Becker, K.-D.; Fritze, H. Electronic and Ionic Transport Mechanisms of Stoichiometric Lithium Niobate at High-Temperatures. *MRS Online Proc. Libr.* **2013**, *1519*, 330. [[CrossRef](#)]
49. Barik, R.; Satpathy, S.K.; Behera, B.; Biswal, S.K.; Mohapatra, R.K. Synthesis and Spectral Characterizations of Nano-Sized Lithium Niobate (LiNbO₃) Ceramic. *Micro Nanosyst.* **2020**, *12*, 1–6. [[CrossRef](#)]
50. Efremov, V.V.; Shcherbina, O.B.; Palatnikov, M.N.; Masloboeva, S.M. Comparative investigation of electrophysical characteristics of ceramic and single crystal LiNbO₃. *J. Phys. Conf. Ser.* **2020**, *1658*, 012010. [[CrossRef](#)]
51. El Bachiri, A.; Bannani, F.; Boussemamti, M. Dielectric and electrical properties of LiNbO₃ ceramics. *J. Asian Ceram. Soc.* **2016**, *4*, 46–54. [[CrossRef](#)]
52. Masoud, M.; Heitjans, P. Impedance Spectroscopy Study of Li Ion Dynamics in Single Crystal, Microcrystalline, Nanocrystalline and Amorphous LiNbO₃. *Defect Diffus. Forum* **2005**, *237–240*, 1016–1021. [[CrossRef](#)]
53. El Bachiri A.; Bannani F.; Boussemamti M. Dielectric and electrical properties of LiNbO₃ ceramics. *J. Asian Ceram. Soc.* **2016**, *4*, 46–54. [[CrossRef](#)]